

# Strong biases in infrared-selected gravitational lenses

Stephen Serjeant

*Department of Physical Sciences, The Open University, Milton Keynes MK7 6AA*

Accepted 2012 February 16. Received 2012 February 16; in original form 2011 November 3

## ABSTRACT

Bright submillimetre-selected galaxies have been found to be a rich source of strong gravitational lenses. However, strong gravitational lensing of extended sources leads inevitably to differential magnification. In this paper I quantify the effect of differential magnification on simulated far-infrared and submillimetre surveys of strong gravitational lenses, using a foreground population of Navarro–Frenk–White plus de Vaucouleurs’ density profiles, with a model source resembling the Cosmic Eyelash and quasi-stellar object J1148+5251. Some emission-line diagnostics are surprisingly unaffected by differential magnification effects: for example, the bolometric fractions of [CII] 158  $\mu\text{m}$  and CO( $J = 1 - 0$ ), often used to infer densities and ionization parameters, have typical differential magnification effects that are smaller than the measurement errors. However, the CO ladder itself is significantly affected. Far-infrared lensed galaxy surveys (e.g. at 60  $\mu\text{m}$ ) strongly select for high-redshift galaxies with caustics close to active galactic nuclei (AGNs), boosting the apparent bolometric contribution of AGN. The lens configuration of IRAS F10214+4724 is naturally explained in this context. Conversely, submillimetre/millimetre-wave surveys (e.g. 500–1400  $\mu\text{m}$ ) strongly select for caustics close to knots of star formation boosting the latter’s bolometric fraction. In general, estimates of bolometric fractions from spectral energy distributions of strongly lensed infrared galaxies are so unreliable as to be useless, unless a lens mass model is available to correct for differential magnification.

**Key words:** galaxies: evolution – galaxies: formation – galaxies: starburst – cosmology: observations – infrared: galaxies.

## 1 INTRODUCTION

Strong gravitational lensing has been widely exploited for studying populations that would otherwise be too faint for detailed study (e.g. Smail et al. 1997; Knudsen et al. 2008), as well as being one of the very few probes capable of mapping the dark matter distributions in the foreground systems (e.g. Gavazzi et al. 2007). Gravitational lenses were originally very difficult to discover: for example, the Cosmic Lens All-Sky Survey (CLASS) observed 11 685 flat-spectrum radio sources, finding 16 gravitational lenses (Myers et al. 2003). More rapid lens discovery has come from exploiting the large public Sloan Digital Sky Survey (SDSS) data base. The Sloan Lens ACS Survey (SLACS) selected lens candidates for *Hubble Space Telescope* (HST) snapshot follow-up from the presence of nebular emission lines at a higher redshift than that of the SDSS galaxy (e.g. Bolton et al. 2006), resulting in nearly 100 published lenses (Auger et al. 2009). The SLACS lens redshifts are  $z < 0.5$  by virtue of their selection criteria, which limits the study of the evolving mass profiles of the lenses, while the background galaxies are by necessity unobscured blue star-forming systems with sufficiently dust-free lines of sight through the foreground lens. Many ongoing

and future applications of gravitational lensing are also limited by sample size (e.g. Treu 2010), and so there are strong drivers both to finding lenses at higher redshifts and to finding lensed systems in greater numbers.

Several authors predicted that the steep bright-end slope of submillimetre source counts, together with the high redshifts of submillimetre-selected galaxies (e.g. Chapman et al. 2005; Eales et al. 2010), would lead to a strong gravitational magnification bias (e.g. Blain 1996; Perrotta et al. 2002; Negrello et al. 2007). Shallow, wide-area submillimetre surveys could therefore be exploited as an extremely efficient means of selecting strong lens events, once the contaminant populations of nearby galaxies and blazars are removed. The millimetre-wave source counts from the South Pole Telescope (SPT) were consistent with this prediction (Vieira et al. 2010), and the prediction was spectacularly confirmed by Negrello et al. (2010), who used an intensive and rapid follow-up of the first data from the *Herschel* Astrophysical Terahertz Large Area Survey (H-ATLAS; Eales et al. 2010) to find that all five of the first lensed galaxy candidates are strong gravitational lenses. The selection efficiency for strong lenses in bright submillimetre surveys approaches an astonishing  $\simeq 100$  per cent. The lens

redshift distribution is expected to peak at  $z \gtrsim 1$ , with lensing systems selected irrespective of the obscuration in the foreground system. The advent of wide-field mapping capabilities at submillimetre and millimetre wavelengths from e.g. *Herschel* Spectral and Photometric Imaging Receiver (SPIRE), Submillimetre Common-User Bolometer Array-2 (SCUBA-2) and SPT allows the discovery of many hundreds of strong lenses (e.g. Cooray et al. 2010; Negrello et al. 2010; Vieira et al. 2010; González-Nuevo et al. 2012). This immediately also affords many opportunities for follow-up imaging and spectroscopic diagnostics of the lensed galaxies (e.g. Lupu et al. 2010; Cooray et al. 2011; Cox et al. 2011; Frayer et al. 2011; Gavazzi et al. 2011; Hopwood et al. 2011; Omont et al. 2011; Riechers et al. 2011; Scott et al. 2011; Valtchanov et al. 2011).

Gravitational lensing is a purely geometrical effect depending on the paths of null geodesics, and is therefore wavelength independent. Nevertheless, different lines of sight have different magnifications in every astrophysical lens. Therefore, if the background source is extended with intrinsic colour gradients, the lensed source may have colours that are different to the unlensed case. This differential magnification could significantly affect broad-band photometry and emission-line diagnostics. Many strong gravitational lenses do not have a well-constrained foreground mass model, so the level and nature of the differential magnification problem in those sources is unknown. Often, a largely unjustified assumption is made, explicitly or implicitly, that differential magnification effects can be neglected, despite the fact that it has long been clear that differential magnification effects are present and must be corrected for (e.g. Blain 1999).

This paper presents a statistical assessment of the level of the differential magnification problem for a wide range of photometric and spectroscopic diagnostics of the physical conditions in gravitationally lensed infrared-luminous galaxies. Section 2 describes the simulation methodology, including the foreground lenses and the adopted background source. Section 3 gives the results of the simulations, demonstrating where it is and where is not appropriate to assume a naive demagnification without differential magnification effects. Section 4 discusses the implications of these results for ongoing follow-up studies of infrared-selected strong gravitational lenses, and the conclusions are summarized in Section 5. This paper assumes a concordance cosmology with a Hubble constant of  $H_0 = 72 \text{ km s}^{-1} \text{ Mpc}^{-1} = 100 h \text{ km s}^{-1} \text{ Mpc}^{-1}$ , a matter density of  $\Omega_M = 0.3$  and a cosmological constant effective energy density of  $\Omega_\Lambda = 0.7$ .

## 2 METHODOLOGY

### 2.1 Simulation details

Differential magnification effects were simulated for a given source at a fixed redshift, seen through a constant comoving population of lenses. The physical parameters of the lens and the source in this case are given in the following subsections. The source plane magnification map, summing over all images  $\sum_i |\mu_i(x, y)|$ , was calculated using the GRAVLENS software (Keeton 2001). The simulation resolution was 0.01 arcsec at this stage. With the source redshift fixed, the differential magnification of the various source components was used to calculate observed spectral energy distributions (SEDs). A selection at a particular wavelength was then imposed: I first assumed that the background source will be considered a strong gravitational lens at that observed wavelength when the total magnification over all source components exceeds a threshold magnification  $\mu \geq 10$ . This was then compared to the case of more

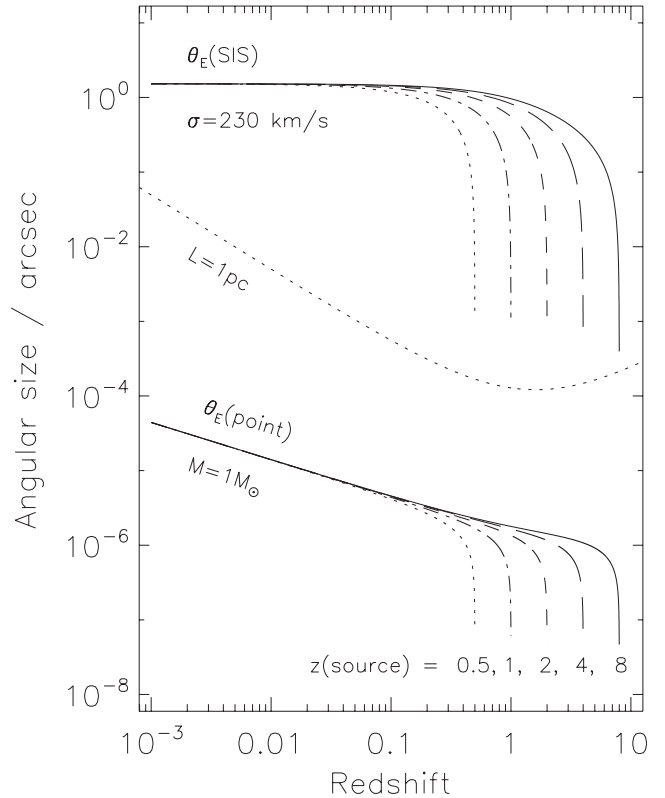


**Figure 1.** The Einstein radius in arcseconds against lens redshift for a singular isothermal sphere with velocity dispersion equal to the SLACS mean of  $230 \text{ km s}^{-1}$  (upper curves; Bolton et al. 2008), and for comparison a  $1 M_\odot$  point lens (lower curves), at source redshifts of 0.5, 1, 2, 4 and 8 (dotted, dash-dot, dashed, long dashed and full lines, respectively). Note that the Einstein radius for the singular isothermal sphere has a much weaker dependence on the lens redshift than the point-mass case, until the lens approaches the source. As a further comparison, the dotted line shows the observed angular size of a fiducial 1 pc proper length. Note that over  $z \simeq 0.5\text{--}3$ , the observed angular sizes are relatively weakly dependent on redshift. The weak dependence on the redshift of both the source sizes and lens critical radii implies that the results in this paper will be only weakly dependent on the background source redshift, notwithstanding differences in rest-frame wavelengths.

moderate magnifications of  $2 < \mu < 5$  at that wavelength. Most of the results presented in this paper are for a  $z = 2$  background source, but it was found that the results depend only weakly on the background source redshift. Differential magnification effects depend on the *relative* angular sizes of the magnification map and the background source. As shown in Fig. 1, angular diameter distance varies only weakly with redshift at  $z \simeq 1\text{--}3$  (see e.g. Serjeant 2010), while the observed critical radii for singular isothermal spheres depend only very weakly on the source and lens redshifts over most of their range (unlike the point mass case). It should therefore be not too surprising that there is no strong dependence on the source redshift in these simulations, notwithstanding changes in rest-frame wavelengths. Section 3.7 presents results for a variety of source redshifts. Most of the results in this paper are based on lenses selected at observed wavelengths of either 60 or 500  $\mu\text{m}$ , representing selection with e.g. *IRAS* and the *Herschel* SPIRE instrument. The 500  $\mu\text{m}$  results for a source at  $z = 2$  are very similar in practice to simulations at 850  $\mu\text{m}$  or 1.4 mm, representing lens selection with e.g. SCUBA-2 or the SPT; this is because all three wavelengths lie well

within the redshifted Rayleigh–Jeans tail. Section 3.7 discusses the dependences on observed wavelength in more detail.

A higher resolution (0.001 arcsec) simulation was then run for the specific case of a lens geometry based on that of IRAS FSC 10214+4724, with a single lens at a redshift of  $z = 0.9$  and a source at  $z = 2.286$ . Finally, calculations were made of flux- or luminosity-limited samples in the context of a particular source count model.

## 2.2 The foreground lenses

The foreground lensing galaxy or galaxies were simulated following SLACS (Bolton et al. 2006). The assumed density profile was the sum of a Navarro–Frenk–White (NFW) profile and a de Vaucouleurs’ profile, which has an azimuthally averaged surface density similar to a singular isothermal ellipsoid (e.g. Gavazzi et al. 2007). Spiral galaxy discs present only 10–20 per cent of the lensing cross-section of elliptical galaxies (e.g. Keeton & Kochanek 1998; Möller, Kitzbichler & Natarajan 2007) so spiral discs are neglected in this analysis. Also neglected for simplicity is the lensing by galaxy groups and clusters, in which it may be rarer to find subarcsecond-scale strong-magnification gradients intercepting the background sources. Nonetheless, the existence of giant optical arcs implies that galaxy clusters can sometimes induce strong magnifications (e.g. Bayliss et al. 2011; Wuyts et al. 2012). In these situations, one might expect differential magnification to be relevant.

The NFW profiles of the elliptical galaxy haloes in this paper had a virial mass equal to the mean SLACS lens mass,  $M_{\text{vir}} = 14h^{-1} \times 10^{12} M_{\odot}$ , and a concentration parameter  $c$  given by

$$c = \frac{9}{1+z} \left( \frac{M_{\text{vir}}}{8.12h^{-1} M_{\odot}} \right)^{-0.14} \quad (1)$$

(Hoekstra et al. 2005, correcting a typographical error in the  $h$  dependence; e.g. Bullock et al. 2001; Gavazzi et al. 2007). The virial radius was set to  $R_{\text{vir}} = 466 h^{-1} \text{ kpc}$ , consistent with

$$M_{\text{vir}} = \frac{4\pi\Delta}{3} \rho_c R_{\text{vir}}^3, \quad (2)$$

where  $\rho_c$  is the critical density and  $\Delta = 119$ . For the de Vaucouleurs’ profile, the effective radius was set to the mean of the SLACS lenses (Gavazzi et al. 2007),  $5.3 h^{-1} \text{ kpc}$ .

For the case of a single lens, the configuration was modelled on the lensed hyperluminous galaxy IRAS F10214+4724 (Rowan-Robinson et al. 1991; Broadhurst & Lehar 1995; Graham & Liu 1995; Serjeant et al. 1995; Eisenhardt et al. 1996), with a background source at a redshift of  $z = 2.286$  (e.g. Brown & Vanden Bout 1991) and a lens at  $z = 0.9$  (e.g. Serjeant et al. 1995, 1998). The ellipticity of the lens, defined as one minus the axis ratio, was set to  $e = 0.21$ , equal to the median value for SLACS lenses (Bolton et al. 2008). No external shear was included as only one angle dependence is necessary to reproduce the SLACS lens morphologies. Under these assumptions, the critical (Einstein) radius is 1.18 arcsec, close to the median value of 1.17 for the SLACS singular isothermal ellipsoid models (table 5 of Bolton et al. 2008).

For the case of a population of lenses, a constant comoving density of these SLACS-like lenses was assumed, whose mass profiles do not evolve except in the variation of concentration parameter (equation 1). No assumptions were made about the comoving density of background sources; instead, the differential lensing statistics were found as a function of the source redshift.

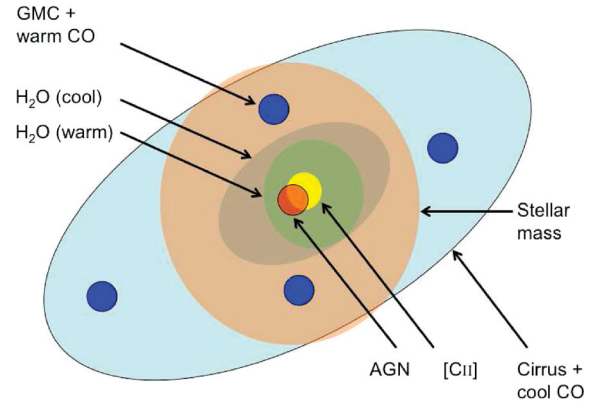


**Figure 2.** A sketch, not to scale, of the emission regions in the model background source described in Section 2.3. The GMCs are embedded in larger warm CO regions.

## 2.3 The background source

### 2.3.1 SMG model

I modelled a submillimetre-selected galaxy (SMG)-like extended background source with a structure resembling that of the Cosmic Eyelash (Swinbank et al. 2010) and the  $z = 6.42$  quasar QSO J1148+5251 (e.g. Walter et al. 2009). The objective is to calculate the differential magnification effects on common emission-line diagnostics (CO, [C II], H<sub>2</sub>O, etc.) and bolometric fractions [active galactic nucleus (AGN), star formation, cirrus] so that the model background galaxy has spatially localized regions and associated SEDs for each of these emission components. Fig. 2 shows a sketch (not to scale) of the components of this simulated galaxy. The source has the following features.

(i) An AGN with a bolometric fraction of 0.3, with an SED from Nenkova et al. (2008a,b), modelled as a circular region with 0.1 kpc radius. The results are not strongly dependent on the AGN torus model chosen, as long as its SED peaks in the rest-frame mid-infrared. The selected model has an AGN and dust torus, incident AGN spectrum AA01, an angular distribution width  $\sigma = 30^\circ$ , a Gaussian angular dust distribution with an equivalent width of  $45^\circ$ , a radial torus thickness of 100 sublimation radii, an average of 14 clumps along a radial equatorial ray, a cloud distribution with a radial dependence of  $r^{-2.0}$  and a visual optical depth of individual clumps of  $\tau_V = 100$ . The torus is simulated as viewed from an inclination angle of  $50^\circ$ .

(ii) An extended cirrus region with a 2.5 kpc major axis, an ellipticity of  $e = 0.4$ , a bolometric fraction of 0.2 and a cirrus SED from Efstathiou, Rowan-Robinson & Siebenmorgen (2000).

(iii) Four extreme giant molecular cloud (GMC) systems, as seen in the Cosmic Eyelash, with a total bolometric fraction of 0.5. The GMCs (assumed identical) are placed randomly into the cirrus region, and have a starburst SED taken from the models of Efstathiou et al. (2000), with an age of 1.7 Myr and an optical depth of  $\tau_V = 100$ . They are modelled as 50 pc radius circular clouds.

(iv) A circular old stellar population with a 2 kpc half-light radius and a de Vaucouleurs’ profile. The 2 Gyr old elliptical SED from the Spitzer Wide-Area Infrared Extragalactic Survey (SWIRE) library (Polletta et al. 2007) is adopted for this component, though for this study it is only necessary that some relatively AGN-free observational proxy is available (e.g. *Spitzer* 3.6  $\mu\text{m}$  fluxes) and that it is possible to subtract the foreground lens (e.g. Hopwood et al. 2011).

(v) A circular [C II] emitting region offset 0.6 kpc from the AGN with radius 0.75 kpc, following the precedent of SDSS QSO J1148+5251. Similarly, the lensed star-forming galaxy MIPS J142824.0+352619 has been argued to contain a [C II]-emitting region extended over kpc scales (Hailey-Dunsheath et al. 2010).

(vi) HCN and HNC emission regions are modelled as two-point sources separated by 80 pc (see Section 3.3).

(vii) Two H<sub>2</sub>O emission regions: a circular ‘warm’ region with a radius of 120 pc and an elliptical ‘cool’ region with a major axis of 1 kpc and an ellipticity and position angle matching the cirrus component. This follows the precedent of Mrk 231 (González-Nuevo et al. 2010; van der Werf et al. 2010).

(viii) A cool molecular gas component tracing the cirrus. The CO emission spectrum was calculated using the RADEX software (van der Tak et al. 2007) using the large velocity gradient (LVG) approximation, assuming that it is comprised of clumps in a background temperature of 8.97 K [i.e.  $2.73(1+z)$  K at  $z = 2.286$ ], with a kinetic temperature of 20 K, an H<sub>2</sub> density of  $100 \text{ cm}^{-3}$  and a CO column density of  $10^{14} \text{ cm}^{-2}$  for each cirrus cloud.

(ix) A warm molecular gas knot with 0.4 kpc radius centred on each GMC. Following the precedent of SDSS QSO J1148+5251, these warm components in total contribute 1/3 of the total CO( $J = 3 - 2$ ) flux. The CO emission of these knots was calculated using the RADEX (van der Tak et al. 2007) LVG model assuming that they are comprised of clumps in a background temperature of 8.97 K [i.e.  $2.73(1+z)$  K at  $z = 2.286$ ], with a kinetic temperature of 45 K, an H<sub>2</sub> density of  $10^4 \text{ cm}^{-3}$  and a CO column density of  $10^{18} \text{ cm}^{-2}$ . There is already good evidence that the higher  $J$  transitions of CO in submillimetre-selected galaxies are much more spatially localized than CO( $J = 1 - 0$ ) (e.g. Ivison et al. 2011).

This model source will be referred to as the SMG model. In the simulations with 0.01 arcsec resolution, the maximum monochromatic magnification of a 500  $\mu\text{m}$ -selected lens at  $z = 2$  for a constant comoving density of lenses is  $\mu = 33$ . Restricting this to configurations with magnifications  $\mu > 10$ , the median (mean) magnification is 11.5 (12.0). At an observed wavelength of 60  $\mu\text{m}$  the flux is dominated by much smaller scale features such as the AGN, so the corresponding numbers are higher: the median (mean) magnification of  $\mu > 10$  sources is 18.5 (21.9), while the maximum monochromatic magnification is 840. The configurations that approach this (possibly unphysical) maximum are nonetheless extremely rare, and the results in this paper are unaffected by excluding all configurations with magnifications of e.g.  $\mu > 100$ . The higher angular resolution simulation discussed in Section 3.6 has a more moderate maximum magnification.

### 2.3.2 Filling factors

The filling factor of emission-line gas in SMGs is far higher than in local galaxies. For example, Carilli et al. (2010) derived a filling factor of 0.5 in the low-excitation gas component of their  $z = 4.05$  SMGs and 0.13 in its higher excitation gas. These values are an order of magnitude or more larger than seen in local galaxies (e.g. McKee & Ostriker 2007). In effect, the clumping of the emission-line gas in high-redshift star-forming galaxies creates a sparse sampling of the morphological distributions defined above. Since the surface filling factor is high, there are unlikely to be problems caused by small number statistics of clumps. The objective is to simulate a high-redshift galaxy, and therefore in the SMG model the emission-line gas is treated as spatially continuous. Any further clumping beyond that already specified is neglected.

## 3 RESULTS

### 3.1 Emission-line diagnostics: [C II] and [O I]

Fig. 3 shows a simulated emission-line diagnostic diagram for a 500  $\mu\text{m}$ -selected SMG model galaxy, lensed with magnifications of  $\mu \geq 10$  and  $2 < \mu < 5$ , with [C II]/ $L_{\text{FIR}}$  plotted against CO( $J = 1 - 0$ )/ $L_{\text{FIR}}$ . This diagram has been used to estimate the density and ionizing radiation environment in star-forming galaxies (e.g. Stacey et al. 2010; Valtchanov et al. 2011). The 500  $\mu\text{m}$  luminosity is taken as a proxy for the far-infrared (FIR) luminosity  $L_{\text{FIR}}$  in the differentially magnified simulated galaxies. It is clear that differential magnification has surprisingly little effect on this diagnostic plot for lensed galaxies. For nearly all lens configurations, differential magnification confines the source to a line almost parallel to the constant density contours. However, the vertical positioning of this track was found to depend on the random positioning of the GMCs in the source model.

If one chooses to use the CO( $J = 4 - 3$ ) line as a proxy for the CO( $J = 1 - 0$ ) line, the smaller emitting regions of CO( $J = 4 - 3$ ) slightly change the differential magnification effects, as shown also in Fig. 3. Table 1 gives the dispersions in the logarithmic bolometric fractions of the emission lines in Fig. 3. The dispersion in  $\log_{10} \text{CO}/L_{\text{FIR}}$  is smaller than the measurement errors of the *H-ATLAS* galaxy ID81, while the standard deviation of  $\log_{10} [\text{C II}]/L_{\text{FIR}}$  is comparable to the measurement errors for ID81 (Valtchanov et al. 2011).

The SHINING survey (Survey with Herschel of the ISM in Nearby Infrared Galaxies; e.g. Sturm et al. 2010) has found that the [O I] 63  $\mu\text{m}$  emission region in M82 is broadly co-spatial with that of the [C II] 158  $\mu\text{m}$  emission on 100–200 pc scales (Contursi et al. 2010; Sturm et al. in preparation). If this is also true of high-redshift star-forming galaxies, the density-sensitive [O I]/[C II] line ratio should be insensitive to differential magnification.

### 3.2 Emission-line diagnostics: CO

Cox et al. (2011) find that the  $z = 4.24$  lensed SMG ID141 has CO spectral line energy distributions (SLEDs) similar in shape to that of the  $z = 4.05$  SMG GN20 (Carilli et al. 2010) and in the  $z = 2.5$  lensed galaxy SMM J16359+6612 (Weiß et al. 2005), though cooler than that of the  $z = 5.3$  millimetre-galaxy AZTEC-3 (Riechers et al. 2010). Could differential magnification skew the CO SLEDs in the lensed galaxies?

Fig. 3 already suggests that the CO ladder is distorted due to the differing spatial extents of the CO emission-line regions in our source model. In this case, the effect on the physical interpretation is much stronger, because of a much smaller dynamic range used for the diagnosis of physical conditions.

Fig. 4 shows the SLEDs for the lensed SMG model source. The SLEDs have been normalized to the CO( $J = 1 - 0$ ) point to remove the overall magnification effects and isolate the differential magnification effects. Clearly the relative proportions of the cool and warm molecular gas components vary strongly, according to the random differential magnification, even for moderate-magnification lenses. Both the 500  $\mu\text{m}$ -selected lenses and 60  $\mu\text{m}$ -selected lenses suffer strong differential magnification effects, though the effects are not identical. There is also a higher probability SLED (the darker bands in Fig. 4) within the overall dispersion that was found to depend on the specific random configuration of the GMCs. The warm molecular gas component is in close physical proximity to the star-forming knots in this model, but this does not necessarily guarantee that



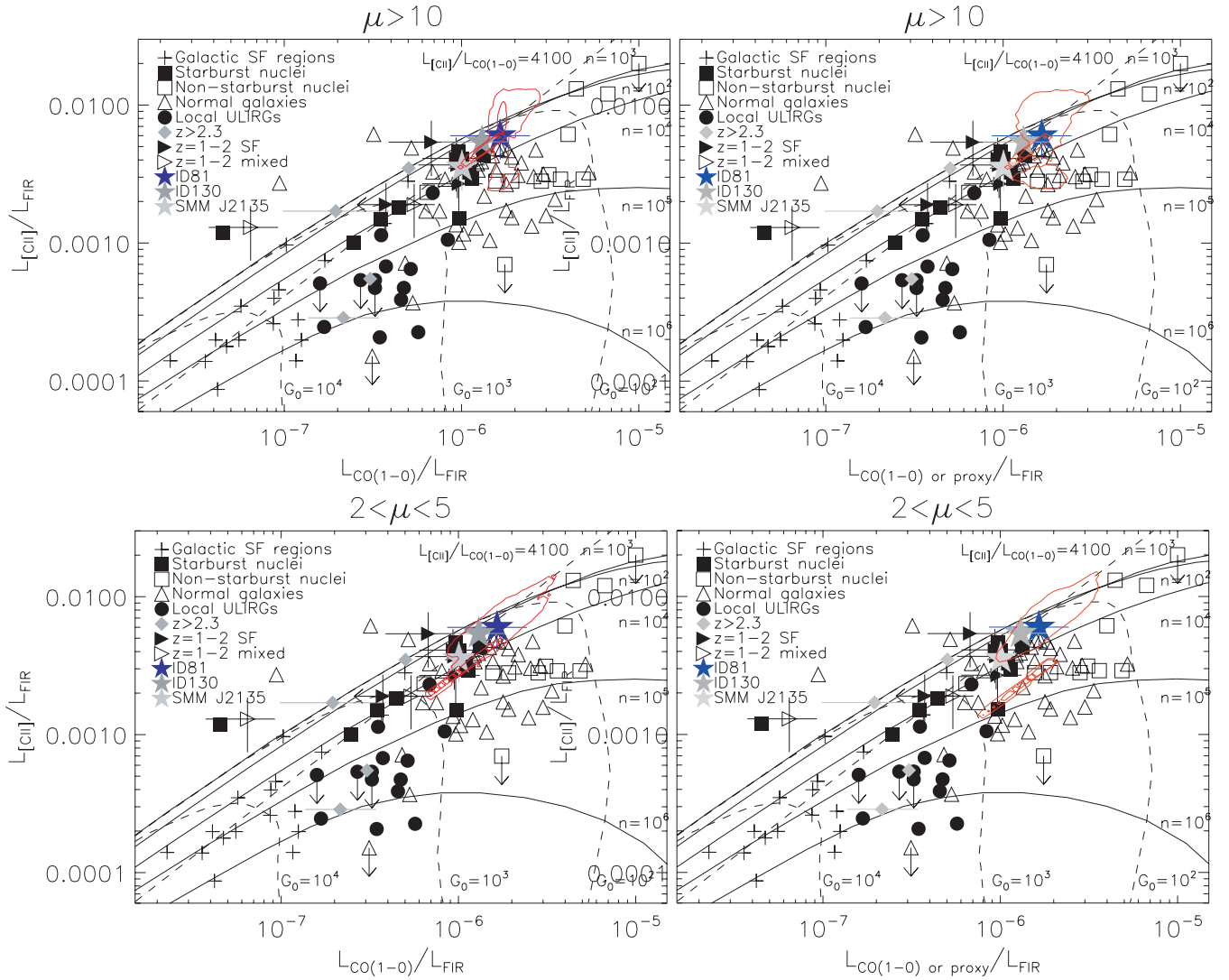


**Figure 3.** Simulated emission-line diagnostic diagram for a 500  $\mu\text{m}$ -selected gravitational lens with a source at  $z = 2$ ; very similar results were found for sources at other redshifts. The underlying value of the line/FIR ratios is taken to be identical to the *H-ATLAS* galaxy ID81 (Valtchanov et al. 2011), while the differentially magnified simulated data points are shown as red contours near the ID81 data point (contours at 68, 95, 99 and 99.9 per cent). The observed data are taken from the compilation in Stacey et al. (2010) and Valtchanov et al. (2011). Also shown are densities and interstellar far-ultraviolet (FUV) flux predictions from Stacey et al. (2010); densities are in units of  $\text{cm}^{-3}$  and the ionizing flux  $F_{\text{FUV}}$  is parametrized as  $G_0 = F_{\text{FUV}}/(1.6 \times 10^{-6} \text{ W m}^{-2})$ . The left-hand panels show the use of the  $\text{CO}(J = 1 - 0)$  line, while the right-hand panels show the use of  $\text{CO}(J = 4 - 3)$  as a proxy for  $\text{CO}(J = 1 - 0)$ . The lower panels show the results for moderate magnifications of  $2 < \mu < 5$ , while the upper panels show high-magnification systems of  $\mu > 10$ . In all four cases, nearly all the contours follow a track that is almost parallel to a constant density diagnostic curve. The vertical positioning of this track was found to depend on the source structure.

**Table 1.** Dispersions in the logarithmic bolometric fractions of key emission-line diagnostics from Fig. 3, for the stated magnifications  $\mu$ .

Ratio	$2 < \mu < 5$	$\mu \geq 10$
$\log_{10}(\text{CO}(J = 1 - 0)/\text{FIR})$	0.16	0.10
$\log_{10}(\text{CO}(J = 4 - 3)/\text{FIR})$	0.15	0.10
$\log_{10}([\text{C II}]/\text{FIR})$	0.17	0.19

the emission from the warm gas component is boosted relative to that from the cool component, even when selecting at an observed wavelength of 500  $\mu\text{m}$ . The  $1\sigma$  dispersion in the apparent  $\text{CO}(J = 6 - 5)$  line [once normalized to  $\text{CO}(J = 1 - 0)$  as in Fig. 4] is 32 per cent of the mean value for 60  $\mu\text{m}$ -selected strong lenses ( $\mu$

$> 10$ ), or 20 per cent of the mean value for 500  $\mu\text{m}$ -selected strong lenses. Even at more moderate magnifications of  $2 < \mu < 5$ , the corresponding dispersions are 29 per cent at 60  $\mu\text{m}$  and 30 per cent at 500  $\mu\text{m}$ .

### 3.3 Emission-line diagnostics: HNC, HCN, $\text{H}_2\text{O}$

Omont et al. (2011) found the bolometric fraction of an  $\text{H}_2\text{O}$  line in the  $z = 2.3$  lensed SMG SDP.17b to be higher than that in Mrk 231, suggestive of a luminous AGN. Van der Werf et al. (2011) detected four rotational  $\text{H}_2\text{O}$  transitions in the  $z = 3.9$  lensed quasar APM 08279+5255, deriving a gas temperature of  $105 \pm 21 \text{ K}$ . Lupu et al. (2011) reported early results from high-density gas tracers in

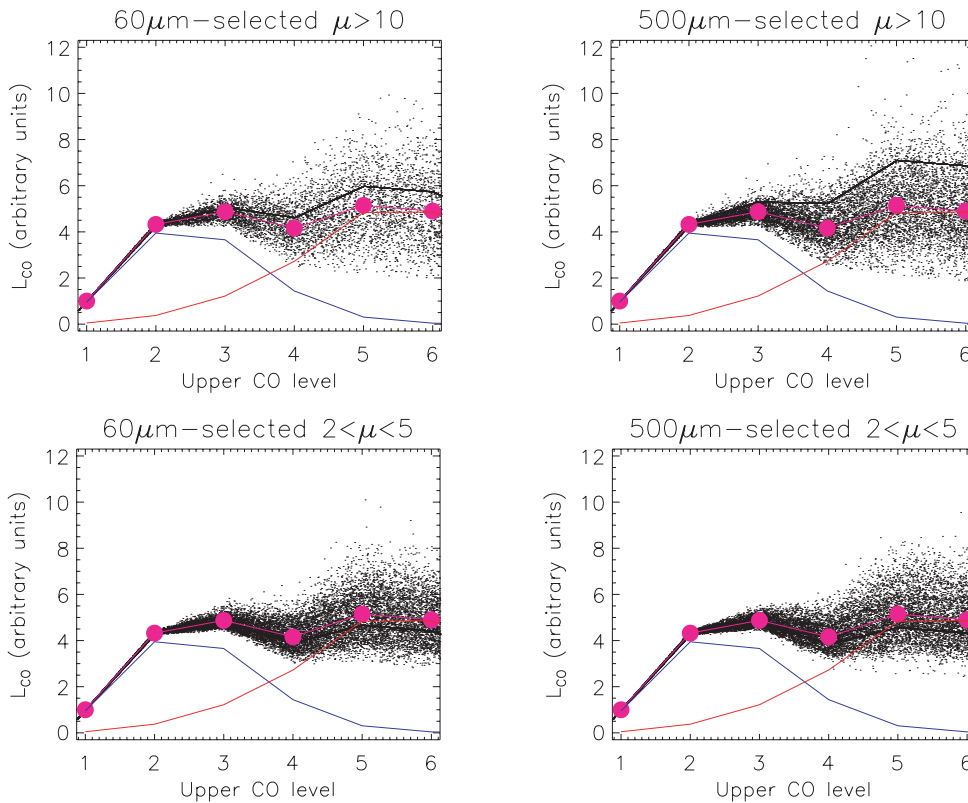


**Figure 4.** Simulated CO SLED for a  $z = 2$  gravitational lens, selected at an observed wavelength of 60  $\mu\text{m}$  (left) and 500  $\mu\text{m}$  (right), using the SMG model as the source. Very similar results were obtained for other source redshifts. The upper panels show the SLEDs for high-magnification lenses with  $\mu > 10$ , while the lower panels show the SLEDs for more moderate magnifications of  $2 < \mu < 5$ ; only a random sparse sample of 2(10) per cent of the lens configurations are shown in the moderate (strong)-magnification case, for clarity. The unlensed cool component is shown as the blue line, while the unlensed warm component is a red line. The magenta line and large symbols show the sum of the unlensed components. The total lensed CO SLEDs are shown as dotted lines, with the dots spaced randomly along each line to avoid overlapping points. In each case, one particularly favoured configuration leads to multiple superimposed dotted lines (i.e. the black line). All SLEDs have been normalized to the CO( $J = 1 - 0$ ) point, to remove the overall effect of magnification and isolate the effects of differential magnification.

lensed SMGs, such as HCN, HNC HCO<sup>+</sup> and <sup>13</sup>CO. Are these observations sensitive to the effects of differential magnification?

The  $J = 1 - 0$  HNC and HCN transitions at rest-frame wavelengths of around 3 mm have very similar critical densities ( $3 \times 10^6 \text{ cm}^{-3}$ ) and so there is a reasonable expectation for these lines to be co-spatial. The HCN:HNC flux ratio is a good diagnostic of whether the emission-line gas is from a photodissociation region (PDR) or an X-ray dissociation region (XDR), e.g., Loenen, Boan & Spaans (2007). The HCN:HCO<sup>+</sup> and HNC:HCO<sup>+</sup> ratios, conversely, are sensitive to densities in PDRs, since HCO<sup>+</sup> has a slightly lower critical density of  $3 \times 10^5 \text{ cm}^{-3}$ . Aalto et al. (2009) find that the  $J = 3 - 2$  HCN and HNC emission in Arp 220 are both confined to a region  $< 350 \text{ pc}$  wide, with most within the central 30 pc. The HCN and HNC emission has therefore been pessimistically modelled in the SMG model source as point sources separated by 80 pc. The simulations confirmed that the differential magnification effect is essentially negligible between these two emission regions.

A similar optimistic situation exists for *moderate* magnification in H<sub>2</sub>O lines. Following the precedent of Mrk 231, the H<sub>2</sub>O emission is modelled as two components, one with a radius of 120 pc, and the other with a major axis of 1 kpc (Section 2.3). These components contribute comparable flux in Mrk 231 at upper energy levels below 200 K, while the warm component dominates at higher temperatures. For 500  $\mu\text{m}$ -selected lenses with *moderate* magnifications of  $2 < \mu < 5$ , the simulations show almost no differential mag-

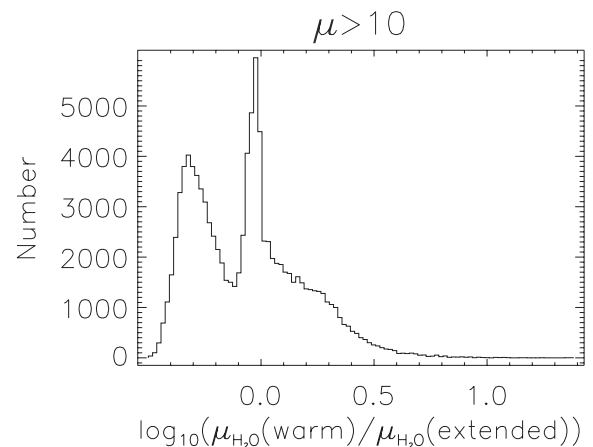


**Figure 5.** Simulated differential magnification of the H<sub>2</sub>O emission regions in the  $z = 2$  SMG model discussed in the text, for a 500  $\mu\text{m}$ -selected gravitational lens with a magnification  $\mu > 10$ .

nification between the two components. Very similar results were obtained for other source redshifts.

However, the situation is not as optimistic for H<sub>2</sub>O lines at magnifications  $\mu > 10$ . These configurations have strong differential magnification effects between these two components, shown in Fig. 5.

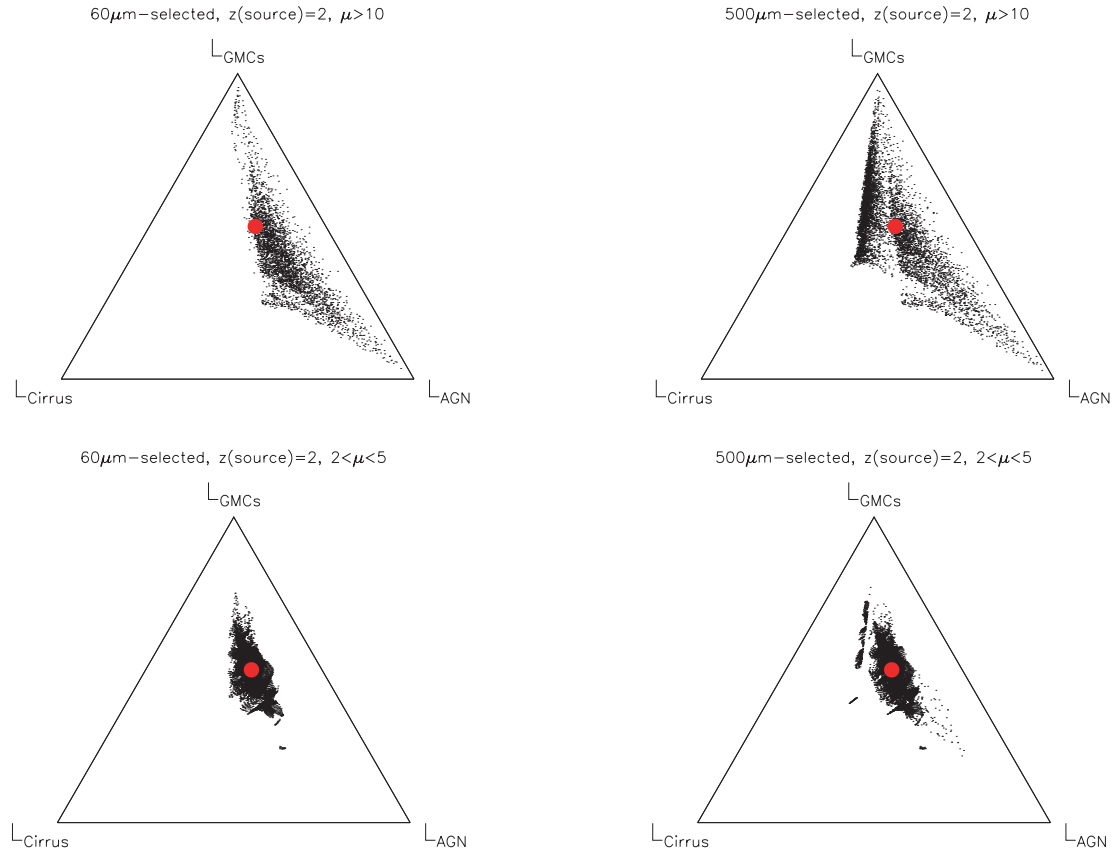


**Figure 6.** Apparent bolometric fractions for the simulated  $z = 2$  SMG model source in Section 2.3, gravitationally lensed by the lens population described in Section 2.2, and then selected at  $60\ \mu\text{m}$  (left) or  $500\ \mu\text{m}$  (right). The upper panels show the results for high-magnification lenses,  $\mu > 10$ ; the lower panels show moderate-magnification lenses,  $2 < \mu < 5$ . The large red dot represents the underlying unlensed source, while the small dots represent the differentially magnified source. The data are represented as a ternary diagram, i.e. the perpendicular distance from any side to the opposite corner is proportional to the bolometric fraction, with 0 per cent on the side and 100 per cent at the corner. Each corner is labelled with the 100 per cent bolometric fraction at that point. Only a random sparse sample of 2(10) per cent of the configurations are plotted in the lower (upper) panels, for clarity.

The figure also shows a tail to high differential magnifications. A similar tail is also present in the magnification ratio of warm  $\text{H}_2\text{O}$  to  $500\ \mu\text{m}$  emission and in that of the warm  $\text{H}_2\text{O}$  to GMC emission. The tail is an alternative interpretation of the  $\text{H}_2\text{O}(2_{02} - 1_{11})$  detection in the lensed *H-ATLAS* galaxy SDP.17b (Omont et al. 2011), since in Mrk 231 about two-third of the luminosity in this line comes from this compact warm component.

The ratios of  $\text{H}_2\text{O}$  to high- $J$  CO transitions have also been argued as a useful diagnostic of PDR versus XDR conditions (e.g. González-Alfonso et al. 2010; van der Werf et al. 2010). In highly magnified lensed systems this will clearly be contingent on the degree that the emissions can be treated as co-spatial.

### 3.4 Apparent bolometric fractions

Broad-band SEDs have long been used to derive the relative bolometric fractions in galaxies of AGN and star formation, via radiative transfer models (e.g. Rowan-Robinson 1980, 2000; Rowan-Robinson & Crawford 1989; Granato, Danese & Franceschini 1996; Green & Rowan-Robinson 1996; Silva et al. 1998, 2011; Efstathiou et al. 2000, 2006; Popescu et al. 2000; Misiriotis et al. 2001; Farrah et al. 2002; Verma et al. 2002; Tuffs et al. 2004; Möllenhoff, Popescu & Tuffs 2006; Popescu et al. 2011). However, it is rare that differen-

tial magnification is explicitly incorporated into SED fits of lensed star-forming galaxies (e.g. Deane et al. 2011).

It is very clear from the lensed SMG model that differential magnification has a strong effect on the apparent bolometric fractions of the continuum components in the model source. Fig. 6 shows the effect of differential magnification on these components in the SMG model source, expressed as a ternary diagram. At each apex, the bolometric fraction of that component is 100 per cent. Along each side, the bolometric fraction of the opposite component is 0 per cent. For example, in the bottom-left corner, the bolometric fraction of the cirrus component would be 100 per cent, while all along the right-hand side the cirrus bolometric fraction is 0 per cent. The bolometric fraction is proportional to the perpendicular distance from a side.

The large red dots in Fig. 6 represent the underlying bolometric fractions in the unlensed source, from Section 2.3. The small dots represent the simulated magnified source, for  $60\ \mu\text{m}$ -selected lenses and for  $500\ \mu\text{m}$ -selected lenses. The cirrus does not have a strong differential magnification, because its physical size is large compared to the caustic sizes in the source plane. However, the GMCs and the AGN are small, and therefore subject to strong differential magnification effects.

In the case of high magnifications ( $\mu > 10$ ), these differential magnification effects are very large. It is clear from Fig. 6 that

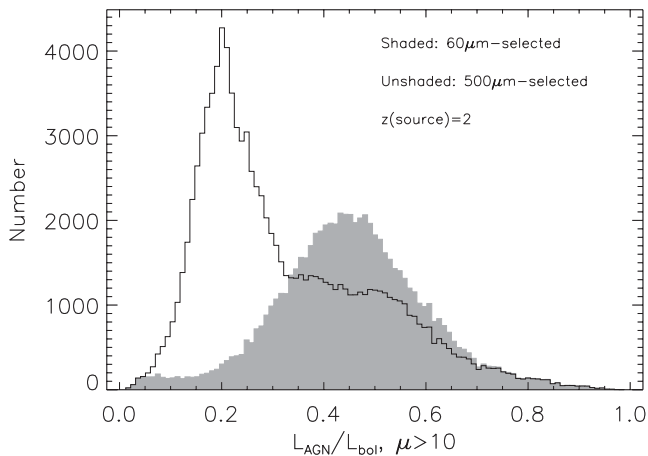


**Figure 7.** Histogram of apparent AGN bolometric luminosity fractions in the simulated  $z = 2$  SMG model source from Section 2.3, and a lens population as described in Section 2.2, for lenses with magnification  $\mu \geq 10$  selected at an observed frame of 60 and 500  $\mu\text{m}$ . The underlying AGN bolometric fraction is 0.3 in this model (Section 2.3). On average, the 60  $\mu\text{m}$  selection over-represents configurations in which the AGN is close to a caustic and has a consequent strong differential magnification. Conversely, 500  $\mu\text{m}$  selection more often has GMCs with the greater magnification. Nevertheless, note that many lens configurations that satisfy the 60  $\mu\text{m}$  lens selection would also satisfy the 500  $\mu\text{m}$  lens selection in this simulation.

without a lens model to correct for differential magnification in strongly lensed systems, the observed bolometric fractions of AGN, starburst and cirrus are so unreliable as to be useless for diagnosing the underlying bolometric fractions.

A curious feature of Fig. 6 is the unoccupied regions for strong lenses ( $\mu > 10$ ). The spatial extent of the cirrus limits its maximum magnification, which corresponds to a diagonal threshold parallel to the right-hand side. However, there are clearly other thresholds also at work: for example, there are no simulated lens configurations with a maximum cirrus bolometric fraction *and* an AGN bolometric fraction of  $\sim 0$  per cent. This reflects the specific spatial configuration of the background source, i.e. there are no configurations in which a GMC is close to a caustic while the AGN is simultaneously distant from all caustic curves.

The different distributions in Fig. 6 demonstrate that the selection wavelength imposes a strong bias on the observed apparent bolometric fractions at high-magnification factors. These differences between the observed-frame selection wavelengths are clearer in Fig. 7, which shows the AGN bolometric fraction for the two selection wavelengths for  $\mu > 10$  lenses. Selecting at 60  $\mu\text{m}$  is sampling  $< 20 \mu\text{m}$  in the rest frame, so one may expect 60  $\mu\text{m}$  selection to favour configurations the AGN torus is close to a caustic in the source plane. This is indeed what is seen in Fig. 7. This also naturally explains the lens configuration of IRAS F10214+4724, in which a cusp appears to lie across the AGN dust torus (Lacy, Rawlings & Serjeant 1998). A similar suggestion was made for other lensed ultraluminous galaxies by Blain (1999). Conversely, 500  $\mu\text{m}$  selection favours the differential magnification of the most luminous small sources at 500  $\mu\text{m}$ , which are the GMCs. Note however that in this simulation, many lens-source configurations that would satisfy the 60  $\mu\text{m}$ -based lens selection, would also satisfy the 500  $\mu\text{m}$ -based lens selection; it is simply that there are additional configurations that are more common in the 500  $\mu\text{m}$  case (Fig. 7).

For moderate-magnification lenses ( $2 < \mu < 5$ ), the observed AGN fraction *is* an unbiased estimator of the underlying value. In

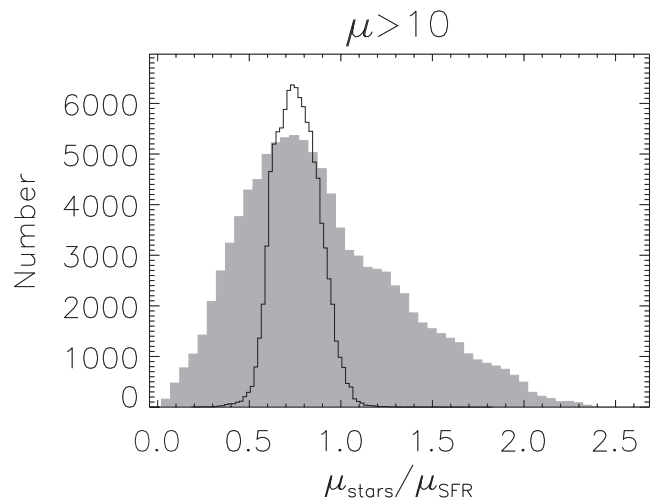


**Figure 8.** The shaded histogram (bin size 0.05) shows the relative magnification factor of the old stars component with that of the star-forming regions in the  $z = 2$  SMG model source with magnifications  $\mu > 10$ . The unshaded histogram (bin size 0.02) gives the result when using the 500  $\mu\text{m}$  luminosity as a proxy for the SFR. Both histograms are for a simulated 500  $\mu\text{m}$ -selected lens.

these simulations, the apparent AGN bolometric fraction for both 60  $\mu\text{m}$ -selected and 500  $\mu\text{m}$ -selected galaxies is roughly normally distributed about the underlying value of 0.3, with a dispersion of 0.03.

### 3.5 The galaxy ‘main sequence’

The suggestion has been made that star-forming galaxies have a characteristic specific star formation rate (SFR), which evolves from  $z = 0$ –2 and then plateaus (e.g. Daddi et al. 2007; Elbaz et al. 2007; Noeske et al. 2007; González et al. 2010; Stark et al. 2009). The scatter in this relationship is around a factor of 2 or more. There has been some discussion as to whether submillimetre-selected galaxies are typical of the population as a whole, or whether they are outliers in this relation (e.g. Tacconi et al. 2006; Hainline et al. 2011; Michałowski et al. 2012). Could differential magnification drive a lensed submillimetre galaxy into appearing as an outlier?

This effect would be strongest at high magnifications, so the  $\mu > 10$  case will be discussed first. Selecting the SMG model lenses at 500  $\mu\text{m}$  and assuming that the old stellar population can be observed at a wavelength at which AGN contributions are negligible and that the foreground lens can be subtracted (e.g. Hopwood et al. 2011), the observed flux ratio of the old stellar population to that of the star-forming regions varies by  $\pm 0.26$  dex ( $1\sigma$ ), as shown in Fig. 8. (This also assumes that one can successfully address problems of the choice of initial mass function, evolutionary synthesis models and star formation histories in estimating the stellar masses; e.g. Michałowski et al. 2012) The median differential magnification ratio is 0.86. Using the 500  $\mu\text{m}$  emission itself as a proxy for the SFR, the dispersion reduces to  $\pm 0.07$  with a median differential magnification ratio of 0.77 (Fig. 8).

For more modest magnifications ( $2 < \mu < 5$ ), the effects are much smaller. The distributions are centred on  $\mu_{\text{stars}}/\mu_{\text{SFR}} = 1$  with a dispersion of 0.14, or 0.06 if using 500  $\mu\text{m}$  luminosity as a proxy for the SFR.

There are two lessons to be drawn from this. First, the specific SFRs can be misleading if the SFR proxy is also the flux at the selection wavelength. This is closely related to the fact that



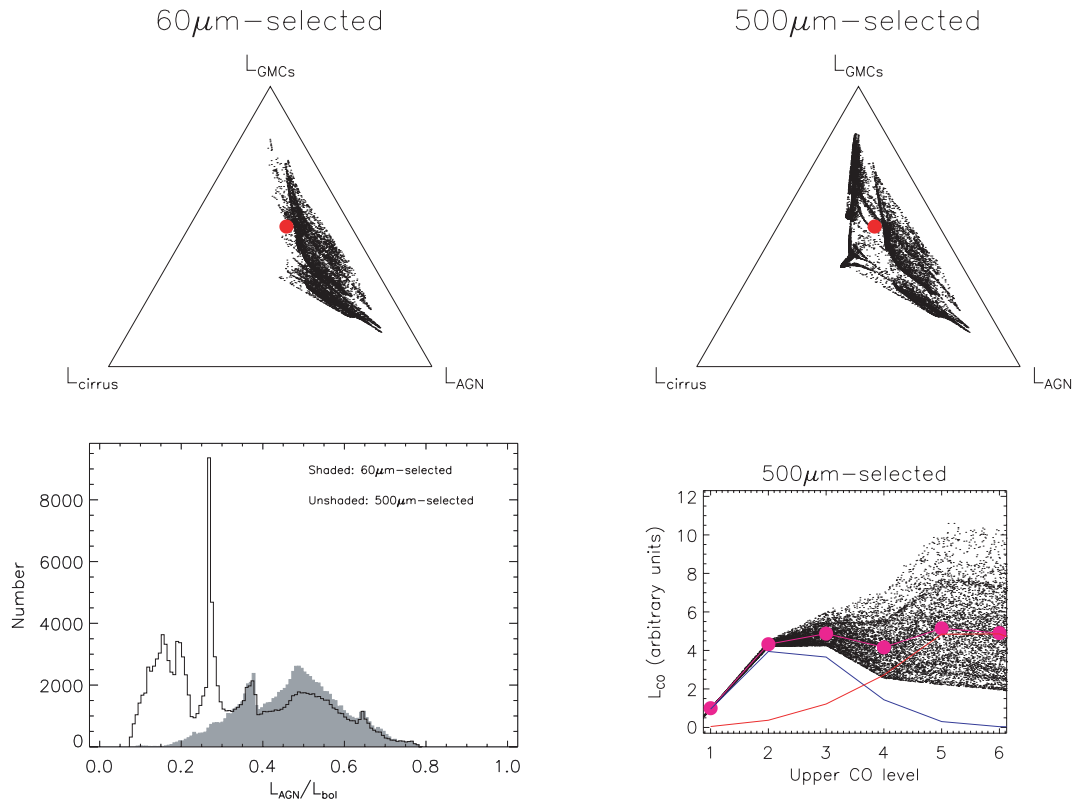


**Figure 9.** A selection of results for simulated high-magnification ( $\mu > 10$ ) lensing configurations for the source and lens redshifts of IRAS FSC 10214+4724. The symbols are as in Figs 4, 6 and 7.

bolometric fractions from the SED shape can be misleading, as noted in the previous section. Secondly, the dispersion induced by differential magnification in this case is comparable to the rather broad dispersion in the galaxy ‘main sequence’. A large offset from this correlation would therefore be unlikely to be attributable to differential magnification.

### 3.6 Results for an IRAS FSC 10214+4724-type lens

How sensitive are the simulations to the angular resolution? The simulation was repeated at a resolution of 0.001 arcsec, i.e. 10 times finer than the lens population above, for a lens at a fixed source redshift of  $z = 2.286$  and a lens at  $z = 0.9$ , modelled on the example of IRAS FSC 10214+4724. The orientation of the lens ellipticity was fixed at an arbitrary value of  $\pi/4$  relative to that of the source. The maximum magnification at an observed wavelength of 500  $\mu\text{m}$  was 17, while at an observed wavelength of 60  $\mu\text{m}$  it was 52. Fig. 9 shows a selection of results for this case. The results are qualitatively similar to the  $z = 2$  lens case with a constant comoving population of lenses; the peaks in the AGN bolometric fraction histograms are due to particular alignments of source structure with cusps in this model. No significant quantitative differences in Fig. 9 were found with an otherwise identical simulation at 0.01 arcsec resolution, justifying the resolution choice of the lens population simulations above, despite the fact that the smallest source structures had been treated as de facto point sources. More results from this lens configuration are found in Serjeant (2011).

### 3.7 Results for other wavelengths and source redshifts: ALMA and SMA

How does differential magnification depend on source redshift and observed wavelength, and how can submillimetre/millimetre-wave

continuum photometry and interferometry illuminate the bolometric fractions?

The discussion up to this point has been restricted to a source redshift of  $z = 2.0$ , with the expectation from Fig. 1 that there should not be a strong dependence on the source redshift, with the exception of a possible dependence on the rest-frame wavelengths being sampled. Confirmation of this can be found in Fig. 10 in which the apparent AGN bolometric fraction is plotted for source redshifts of  $z = 1$  and  $z = 4$ .

Most of the results in this paper for 500  $\mu\text{m}$ -selected galaxies apply equally to 1.4 millimetre-selected galaxies, since both wavelengths usually lie well within the Rayleigh–Jeans tail. However, at sufficiently high redshifts, this situation must change. Fig. 11 presents a comparison of the monochromatic magnifications at 500  $\mu\text{m}$  and 1.4 mm for source redshifts of  $z = 1, 2$  and 4. Only at the highest redshifts and high magnifications are there appreciable differences in the monochromatic magnification factors. A corollary is that e.g. 870  $\mu\text{m}$  submillimetre array (SMA) follow-ups of 500  $\mu\text{m}$ -selected lenses will be accurately recovering the 500  $\mu\text{m}$  magnifications and morphologies, provided that the 500  $\mu\text{m}$  pass-band is not close to the peak of the SED, or that the magnification factor is not large. Similarly, SMA mapping will almost always recover the 1.4 mm morphologies and magnifications. Atacama Large Millimetre Array (ALMA) mapping of submillimetre/millimetre-wave-selected strongly lensed galaxies will also recover the morphologies and magnifications at the selected wavelength, provided that both the ALMA band and the selection wavelength are on the Rayleigh–Jeans tail (or that the ALMA band and the selection wavelengths are similar).

However, it does not necessarily follow that single-band photometry is a good tracer of any particular component of the background

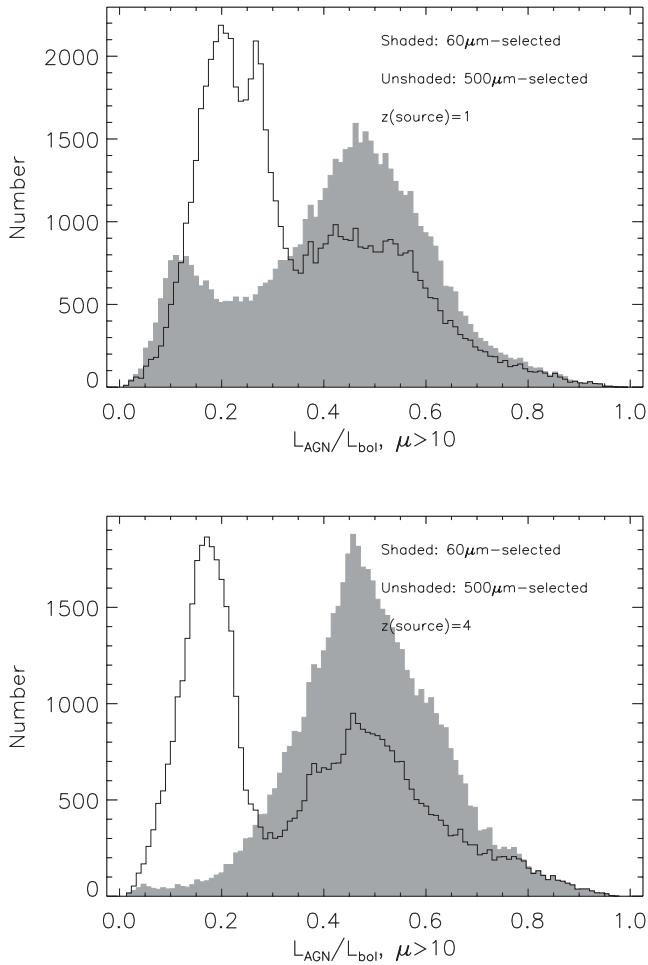


**Figure 10.** The apparent AGN bolometric fractions for a source redshift of  $z = 1.0$  and  $z = 4.0$ , for  $\mu > 10$  lensed galaxies selected at  $60 \mu\text{m}$  (grey) and  $500 \mu\text{m}$  (open). Note the similarity to Fig. 7.

galaxy. Fig. 12 correlates the monochromatic magnification factors at selected wavelengths with the magnifications of the AGN, starburst and cirrus components. As one might expect, mid-infrared rest-frame photometry is a good tracer of the magnification of the AGN component. The magnification of the cirrus component is well traced by photometry on the Rayleigh–Jeans tail. The starburst component, however, appears not to be well traced by any single monochromatic photometric measurement. In order to decouple the starburst and cirrus components, one must either obtain more extensive coverage of the FIR to submillimetre/millimetre-wave SED, or obtain resolved imaging to decouple the FIR-luminous components.

### 3.8 Source count model predictions

One potential bias not accounted for in the discussion so far is the effect of the slope of the luminosity function. As the slope steepens, the magnification bias is stronger. Might one expect more pathological lens configurations as one samples populations progressively brighter than the break luminosity  $L_*$ ?

Lapi et al. (2011) recently presented constraints on the evolving  $100 \mu\text{m}$  rest-frame luminosity function of submillimetre-selected galaxies. Their  $z = 2.4$ – $4$  luminosity function and their toy model that fits it are both consistent with a Schechter function with a

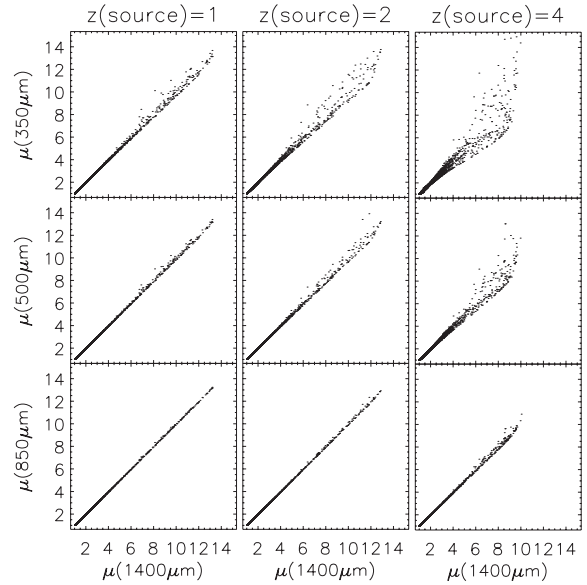


**Figure 11.** The monochromatic magnification factors at observed wavelengths of  $350 \mu\text{m}$ ,  $500 \mu\text{m}$ ,  $850 \mu\text{m}$  and  $1.4 \text{ mm}$ , for source redshifts of  $z = 1$ ,  $z = 2$  and  $z = 4$  and lens redshift of half the source redshift. Note that the magnifications are essentially identical until the passband moves off the Rayleigh–Jeans tail.

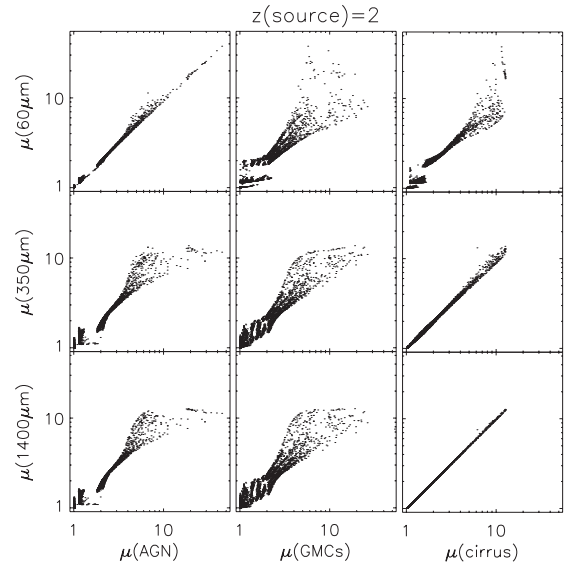


**Figure 12.** The monochromatic magnification factors compared to the magnifications of specific components, for an example source at  $z = 2$  and a lens at  $z = 1$ . Note that the AGN is well traced by rest-frame mid-infrared photometry, and cirrus by photometry on the Rayleigh–Jeans tail, but that there is no single monochromatic tracer for star-forming regions. Measuring this component, and decoupling it from the extended cirrus component, requires resolved imaging in the submillimetre or millimetre wavelengths.

faint-end slope of  $-1.46$ . This luminosity function was assumed to hold at  $z = 4$ . Submillimetre galaxies were sampled from this distribution and magnified by the constant comoving density of lenses described above. The results are shown in Fig. 13. It is clear that the qualitative results of the magnification simulations in Section 3.4 are unaffected.

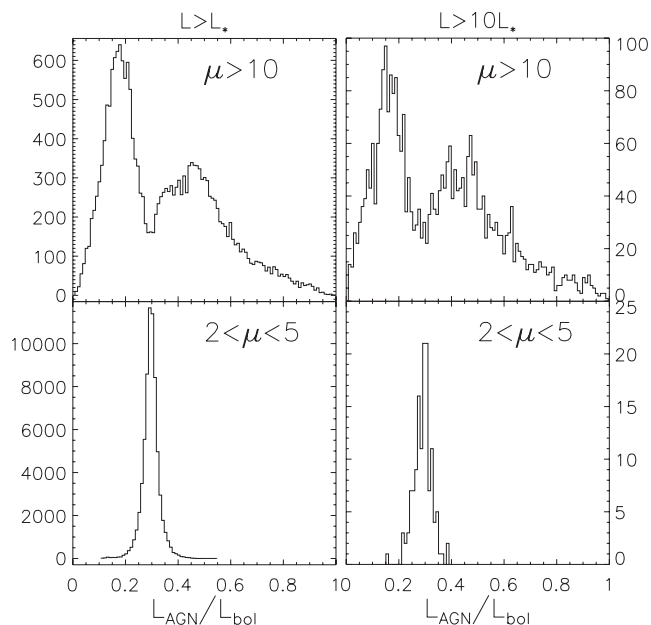


**Figure 13.** Histograms of simulated AGN bolometric fractions for  $z = 4$  lensed galaxies, selected at an observed wavelength of  $500 \mu\text{m}$  from a  $100 \mu\text{m}$  rest-frame Schechter function with a faint-end slope of  $-1.46$ . Samples are shown brighter than  $L_*$  (left) or  $10L_*$  (right). The underlying bolometric fraction is 0.3. The moderate-magnification ( $2 < \mu < 5$ ) and strong-magnification ( $\mu > 10$ ) cases are shown. Qualitatively similar results are found at other source redshifts, and the results are only weakly dependent on the faint-end slope of the luminosity function.

## 4 DISCUSSION

The obvious underlying principle of these simulations is that spatially compact regions are prone to differential magnification, particularly in the more strongly magnified systems, while spatially extended regions are less prone to this bias. For the specific SMG model galaxy and foreground lens population discussed in this paper, this underlying principle leads to several specific conclusions with clear implications for the follow-ups of infrared-selected strong gravitational lens systems.

It is particularly clear that for high-magnification lenses ( $\mu > 10$ ), the observed selection wavelength has a strong effect on the distribution of relative bolometric fractions. Radiative transfer models are an extremely effective and well-established route to decomposing the relative bolometric fractions of ultraluminous galaxies (e.g. Rowan-Robinson 1980; Rowan-Robinson & Crawford 1989; Granato et al. 1996; Green & Rowan-Robinson 1996; Silva et al. 1998, 2011; Efstathiou et al. 2000; Popescu et al. 2000, 2011; Misiriotis et al. 2001; Tuffs et al. 2004; Möllenhoff et al. 2006), but in the case of strong infrared-selected lenses with magnifications  $\mu > 10$ , differential magnification is so strong as to make integrated SEDs completely unreliable in estimating relative bolometric fractions in lensed galaxies, unless a lens model is available to determine the differential magnification (cf. e.g. Granato et al. 1996; Rowan-Robinson 2000; Farrah et al. 2002; Verma et al. 2002; Efstathiou 2006). Nevertheless, for more moderate lensed systems ( $2 < \mu < 5$ ), the underlying bolometric fractions can still be reliably determined even when neglecting the effects of differential magnification.

These results are robust to the assumed configuration of the components in the background source. The background source would have to be broadly homogeneous in order to avoid strong differential magnification effects. One way to do this would be to argue

that the number of GMC regions is much larger, perhaps numbering several tens to resemble those in the Milky Way or M31 (e.g. Sheth et al. 2008). However, there is little evidence that star formation in high-redshift infrared-luminous galaxies very closely resembles  $z = 0$  spiral discs. Furthermore, an active nucleus will inevitably create a mid-infrared/FIR colour gradient in the background source.

Despite the lens magnification, the prospects are excellent for using e.g. the  $[\text{C II}]/\text{FIR}$  versus  $\text{CO}/\text{FIR}$  line diagnostic diagram (e.g. Stacey et al. 2010; Valtchanov et al. 2011) for determining the physical conditions in the emission-line gas. The line ratios of  $\text{HCN}/\text{HNC}$  and  $[\text{O II}]/[\text{C II}]$  appear to be particularly insensitive to differential magnification. The differential magnification effects on the  $\text{H}_2\text{O}$  lines can be neglected for moderate magnifications ( $2 < \mu < 5$ ) but not for higher magnifications. Other line diagnostics are nonetheless prone to differential magnification, such as the CO ladder, even for low-magnification systems ( $\mu > 2$ ). For example, the line ratio  $\text{CO}(J = 6 - 5)/\text{CO}(J = 1 - 0)$  has a  $1\sigma$  dispersion of  $\sim 30$  per cent due purely to the effects of differential magnification for all the simulations presented in this paper. One might try to avoid these strong differential magnification effects by arguing that the CO transitions are spatially co-located, but this is unlikely to be the case. Even in local star-forming galaxies, the low- $J$  transitions of CO are more spatially extended than higher transitions (e.g. Paglione et al. 2004; Sakamoto et al. 2011), and evidence is accumulating of similar trends in high-redshift infrared-luminous galaxies (e.g. Ivison et al. 2011).

There is therefore a set of photometric and spectroscopic diagnostics that do not require a detailed lens magnification model, and others for which such a model is beneficial or even essential. Snapshot observations with ALMA, e-Merlin, the expanded Very Large Array (eVLA), the Plateau de Bure Interferometer (PdBI) and/or the Combined Array for Research in Millimetre-Wave Astronomy (CARMA) of lens candidates from *Herschel*, *Planck*, SPT or SCUBA-2 would easily establish whether a system is in a low-magnification (e.g.  $\mu \simeq 2$ ) or high-magnification (e.g.  $\mu > 10$ ) regime, because the image separation would be enough to constrain the lens magnification. Ground-based optical or near-infrared imaging may also assist, but the very red colours of some lensed submillimetre galaxies (e.g. Hopwood et al. 2011) suggest that *HST* near-infrared observations will often be required to detect the background source. High-resolution submillimetre/millimetre-wave interferometry is also the only way to decouple the lensed star-forming knots from the lensed extended submillimetre emission (Figs 11 and 12), giving an additional clear rationale for ALMA and SMA follow-ups.

This paper has focused on FIR to millimetre-wave emission-line diagnostics, but similar considerations may be applicable to rest-frame optical and ultraviolet lines. The presence of Lyman  $\alpha$  emission in some heavily obscured submillimetre-selected galaxies (e.g. Chapman et al. 2005) necessarily requires highly anisotropic obscuration, perhaps through the evacuation of cavities via supernova-driven winds. Differential magnification may clearly affect the occurrence of nebular emission lines in lensed infrared-luminous galaxies. If the nebular lines are close to or coincident with the GMC components in the galaxy, then there may be examples of submillimetre/millimetre-wave-selected lensed infrared-luminous galaxies in which the UV/optical emission lines are more easily detectable. A similar consideration may explain the strong narrow AGN emission lines in IRAS FSC 10214+4724, and differential magnification may also help explain their unusual line ratios and widths (e.g. Serjeant et al. 1998). However, it does *not* necessarily follow that close proximity leads to enhancement. The model GMCs

have a 50 pc radius, embedded in a warm CO knot of 400 pc radius, yet the high- $J$  CO lines do not necessarily share the total magnification boost of the GMCs. Similarly, extended Lyman  $\alpha$  nebulosity may not necessarily be as boosted as the continuum sources at the selection wavelength.

If the images of the background source are resolved and a lens mass model can be constructed, one might alternatively choose to regard differential magnification as an asset, rather than a problem. Lensing conserves surface brightness, so high-magnification regions also have high angular magnification. The presence of caustics in the foreground lens magnification could be used to make uniquely high angular resolution reconstructions of active nuclei or star-forming regions in infrared-luminous galaxies.

## 5 CONCLUSIONS

In infrared-selected gravitational lenses of any magnification  $\mu > 2$ , the CO ladder is strongly distorted by differential magnification. The bolometric fractions of the FIR [C II] and [O I] lines are also affected by differential magnification, but the distortion is not typically sufficient to alter the physical interpretation. Similarly, differential magnification should not typically move a galaxy more than a factor of about 2 from its position on the proposed galaxy ‘main sequence’. For moderate-magnification lenses ( $2 < \mu < 5$ ), the FIR H<sub>2</sub>O, HCN and HNC lines are broadly unaffected by differential magnification, and the broad-band SED-based decompositions of bolometric contributions should be reliable. However, for strong lenses ( $\mu > 10$ ) in the absence of a foreground mass model, the H<sub>2</sub>O lines are significantly distorted, and unless a detailed lens model can be constructed, the apparent bolometric contributions of AGN, GMCs and cirrus derived from the SEDs are so unreliable as to be useless.

## NOTE ADDED IN PROOF

After this paper was accepted, Hezaveh et al. (2012) presented a complementary study of differential magnification for a source population with components varying in physical sizes. They found that highly-magnified populations over-represent compact physical components in good agreement with Section 3.4 of this paper.

## ACKNOWLEDGMENTS

This research was supported by STFC under grant ST/G002533/1. The author would like to thank Shane Bussmann, Loretta Dunne, Rob Ivison, Roxana Lupu, Mattia Negrello, Douglas Scott, Ian Smail and Glenn White for stimulating discussions, and the anonymous referee for very helpful and timely comments.

## REFERENCES

Aalto A. et al., 2009, *A&A*, 493, 481  
 Auger M. W. et al., 2009, *ApJ*, 705, 1099  
 Bayliss M. B. et al., 2011, *ApJ*, 727, L26  
 Blain A., 1996, *MNRAS*, 283, 1340  
 Blain A., 1999, *MNRAS*, 304, 669  
 Bolton A. S. et al., 2006, *ApJ*, 638, 703  
 Bolton A. S. et al., 2008, *ApJ*, 682, 964  
 Broadhurst T., Lehar J., 1995, *ApJ*, 450, L41  
 Brown R. L., Vanden Bout P. A., 1991, *AJ*, 102, 1956  
 Bullock J. S. et al., 2001, *MNRAS*, 321, 559  
 Carilli C. L. et al., 2010, *ApJ*, 714, 1407  
 Chapman S. C. et al., 2005, *ApJ*, 622, 772  
 Contursi A. et al., 2010, *Proc. Herschel First Results Symp.* (ESLAB 2010)

Cooray A. et al., 2010, preprint (arXiv:1007.3519)  
 Cooray A. et al., 2011, *ApJ*, 732, L35  
 Cox P. et al., 2011, *ApJ*, 740, 63  
 Daddi E. et al., 2007, *ApJ*, 670, 156  
 Deane R. P., Rawlings S., Marshall P., Heywood I., Klöckner H.-R., Grainge K., Mauch T., Serjeant S., 2011, *MNRAS*, submitted  
 Eales S. A. et al., 2010, *PASP*, 122, 499  
 Efstathiou A., 2006, *MNRAS*, 371, L70  
 Efstathiou A., Rowan-Robinson M., Siebenmorgen R., 2000, *MNRAS*, 313, 734  
 Eisenhardt P., Armus L., Hogg D. W., Soifer B. T., Neugebauer G., Werner M. W., 1996, *ApJ*, 461, 72  
 Elbaz D. et al., 2007, *A&A*, 468, 33  
 Farrah D., Serjeant S., Efstathiou A., Rowan-Robinson M., Verma A., 2002, *MNRAS*, 335, 1163  
 Frayer D. T. et al., 2011, *ApJ*, 726, L22  
 Gavazzi R. et al., 2007, *ApJ*, 667, 176  
 Gavazzi R. et al., 2011, *ApJ*, 738, 125  
 González V. et al., 2010, *ApJ*, 713, 115  
 González-Alfonso E. et al., 2010, *A&A*, 518, L43  
 González-Nuevo J. et al., 2012, *ApJ*, 749, 65  
 Graham J. R., Liu M. C., 1995, *ApJ*, 449, L29  
 Granato G. L., Danese L., Franceschini A., 1996, *ApJ*, 460, L11  
 Green S. M., Rowan-Robinson M., 1996, *MNRAS*, 279, 884  
 Hailey-Dunsheath S. et al., 2010, *ApJ*, 714, L162  
 Hainline L. et al., 2011, *ApJ*, 740, 96  
 Hezaveh Y. D., Marrone D. P., Holder G. P., 2012, preprint (arXiv:1203.3267)  
 Hoekstra H., Hsieh B. C., Yee H. K. C., Lin H., Gladders M. D., 2005, *ApJ*, 635, 73  
 Hopwood R. et al., 2011, *ApJ*, 728, L4  
 Ivison R. J. et al., 2011, *MNRAS*, 412, 1913  
 Keeton C. R., 2001, preprint (astro-ph/0102340)  
 Keeton C. R., Kochanek C. S., 1998, *ApJ*, 495, 157  
 Knudsen K. K. et al., 2008, *MNRAS*, 384, 1161  
 Lacy M., Rawlings S., Serjeant S., 1998, *MNRAS*, 299, 1220  
 Lapi A. et al., 2011, *ApJ*, 742, 24  
 Loenen A. F., Boan W. A., Spaans M., 2007, in Chapman J. M., Baan W. A., eds, *Proc. IAU Symp. Vol. 242, Astrophysical Masers and their Environments*. Cambridge Univ. Press, Cambridge, p. 462  
 Lupu R. et al., 2010, *ApJ*, preprint (arXiv:1009.5983)  
 Lupu R. et al., 2011, in Cernicharo J., Bachiller R., eds, *Proc. IAU Symp. Vol. 280, The Molecular Universe*. Cambridge Univ. Press, Cambridge  
 McKee C. F., Ostriker E. C., 2007, *ARA&A*, 45, 565  
 Michałowski M. et al., 2012, *A&A*, 541, 85  
 Misiriotis A., Popescu C. C., Tuffs R., Kylafis N. D., 2001, *A&A*, 372, 775  
 Möllenhoff C., Popescu C. C., Tuffs R. J., 2006, *A&A*, 456, 941  
 Möller O., Kitzbichler M., Natarajan P., 2007, *MNRAS*, 379, 1195  
 Myers S. T. et al., 2003, *MNRAS*, 341, 1  
 Negrello M. et al., 2007, *MNRAS*, 377, 1557  
 Negrello M. et al., 2010, *Sci*, 330, 800  
 Nenkova M., Sirocky M. M., Ivesić Ž., Elitzur M., 2008a, *ApJ*, 685, 147  
 Nenkova M., Sirocky M. M., Ivesić Ž., Elitzur M., 2008b, *ApJ*, 685, 160  
 Noeske K. G. et al., 2007, *ApJ*, 660, L43  
 Omont A. et al., 2011, *A&A*, 530, L3  
 Paglione T. A. D. et al., 2004, *ApJ*, 611, 835  
 Perrotta F., Baccigalupi C., Bartelmann M., De Zotti G., Granato G. L., 2002, *MNRAS*, 339, 445  
 Polletta M. et al., 2007, *ApJ*, 663, 81  
 Popescu C. C., Misiriotis A., Kylafis N. D., Tuffs R. J., Fischera J., 2000, *A&A*, 362, 138  
 Popescu C. C., Tuffs R. J., Dopita M. A., Fischera J., Kylafis N. D., Madore B. F., 2011, *A&A*, 527, 109  
 Riechers D. A. et al., 2010, *ApJ*, 720, L131  
 Riechers D. A. et al., 2011, *ApJ*, 733, L12  
 Rowan-Robinson M., 1980, *ApJS*, 44, 403  
 Rowan-Robinson M., 2000, *MNRAS*, 316, 885  
 Rowan-Robinson M., Crawford J., 1989, *MNRAS*, 238, 523



- Rowan-Robinson M. et al., 1991, *Nat*, 351, 719  
 Sakamoto K. et al., 2011, *ApJ*, 735, 19  
 Scott K. S. et al., 2011, *ApJ*, 733, 29  
 Serjeant S., 2010, *Observational Cosmology*. Cambridge Univ. Press, Cambridge  
 Serjeant S., 2011, in Tuffs R. J., Popescu C. C., eds, *Proc. IAU Symp. Vol. 284, The Spectral Energy Distribution of Galaxies*. Cambridge Univ. Press, Cambridge, in press  
 Serjeant S., Lacy M., Rawlings S., King L. J., Clements D. L., 1995, *MNRAS*, 276, L31  
 Serjeant S. et al., 1998, *MNRAS*, 298, 321  
 Sheth K. et al., 2008, *ApJ*, 675, 330  
 Silva L., Granato G. L., Bressan A., Danese L., 1998, *ApJ*, 509, 103  
 Silva L. et al., 2011, *MNRAS*, 410, 2043  
 Smail I. et al., 1997, *ApJ*, 490, L5  
 Stacey G. et al., 2010, *ApJ*, 724, 957  
 Stark D. P. et al., 2009, *ApJ*, 697, 1493  
 Sturm E. et al., 2010, *ApJ*, 733, L15  
 Swinbank A. M. et al., 2010, *Nat*, 464, 733  
 Tacconi L. J. et al., 2006, *ApJ*, 640, 228  
 Treu T., 2010, *ARA&A*, 48, 87  
 Tuffs R. J., Popescu C. C., Völk H. J., Kyfalis N. D., Dopita M. A., 2004, *A&A*, 419, 821  
 Valtchanov I. et al., 2011, *MNRAS*, 415, 3473  
 van der Tak F. F. S. et al., 2007, *A&A*, 468, 627  
 van der Werf P. P. et al., 2010, *A&A*, 518, L42  
 van der Werf P. P. et al., 2011, *ApJ*, 741, L38  
 Verma A., Rowan-Robinson M., McMachon R., Efstathiou A., 2002, *MNRAS*, 335, 574  
 Vieira J. D. et al., 2010, *ApJ*, 719, 763  
 Walter F. et al., 2009, *Nat*, 457, 699  
 Weiß A., Henkel C., Downes D., Walter F., 2005, *A&A*, 409, L41  
 Wuyts E. et al., 2012, *ApJ*, 745, 86

This paper has been typeset from a  $\text{\LaTeX}$  file prepared by the author.